Revealing Short- and Long-range Li-ion diffusion in Li_2MnO_3 from finite-temperature dynamical mean field theory

Alex Taekyung Lee,[1,2] Kristin A. Persson,[3,4] and Anh T. Ngo[1,2]

[1] *Department of Chemical engineering, University of Illinois at Chicago, Chicago, IL 60608, USA*
[2] *Materials Science Division, Argonne National laboratory, Lemont, IL 60439, USA*
[3] *Environmental Energy Technologies Division, Lawrence Berkeley National Laboratory, Berkeley, California 94720, United States*
[4] *Department of Materials Science and Engineering, University of California Berkeley, Berkeley, California 94704, United States*

(Dated: May 29, 2026)

Li_2MnO_3 is a key component of Li-excess layered cathodes of the form $(1-x)$, $LiMO_2+x$, Li_2MnO_3 (M = Mn, Ni, Co, ...), yet its role in setting Li-ion transport limitations remains under debate. Here we combine DFT+U, finite-temperature DFT+DMFT with a continuous-time quantum Monte Carlo impurity solver, and nudged-elastic-band (NEB) calculations to study Li^+ migration in paramagnetic Li_2MnO_3 in the presence of a single Li vacancy. Evaluating DMFT total energies along the DFT+U NEB geometries reveals that dynamical correlations strongly renormalize the lowest-barrier processes, reducing the activation energies to $E_a = 0.18$ eV for the shortest-range hop and $E_a = 0.50$ eV for the next-lowest (transport-controlling) step. The 0.18 eV barrier quantitatively reproduces the short-range activation energy from μ^+SR, while the 0.50 eV barrier is consistent with the long-range transport scale extracted from ac-impedance measurements. This single-vacancy, paramagnetic DMFT description thus provides a unified interpretation of local and macroscopic probes without invoking clustered vacancy configurations or strong extrinsic disorder, consistent with nearly stoichiometric Li_2MnO_3 powders. More broadly, our results highlight finite-temperature dynamical correlations as an essential ingredient for predicting ionic migration energetics in correlated oxide electrodes.

I. INTRODUCTION

Rising energy- and power-density targets for lithium-ion batteries have intensified the need for cathode materials that combine high capacity with strong rate capability [1–4]. Within Li-excess layered oxides, Li_2MnO_3 is a key building block in composite cathode chemistries of the form $(1-x)$, $LiMO_2+x$, Li_2MnO_3 (M = Mn, Ni, Co, ...) and is widely used to access high operating voltages (∼4.4–5.0 V) at low cost [5–8]. Understanding the mechanisms and limitations of Li-ion mobility in Li_2MnO_3 is therefore crucial for interpreting rate limitations in Li-rich layered cathodes and for guiding the design of improved electrode architectures.

Experimental estimates of Li-ion migration in Li_2MnO_3 exhibit a pronounced dependence on the probe and the associated length scale [9–11]. At the microscopic (local) scale, μ^+SR measurements on nearly stoichiometric Li_2MnO_3 powders over 2–500 K report a low activation energy, $E_a = 0.156$ eV, for short-range Li jumps in the high-temperature paramagnetic regime ($T \gg T_N$) [10]. In contrast, ac-impedance measurements on Li_2MnO_3 ceramic powders yield a substantially larger apparent barrier, $E_a \approx 0.46$ eV, for long-range Li-ion transport [9]. Taken together, these results suggest a hierarchy of activation energies for local versus percolating Li motion even in nominally pristine Li_2MnO_3.

First-principles nudged-elastic-band (NEB) studies based on density functional theory (DFT)+U have provided valuable insight into the topology of Li-ion migration pathways in Li_2MnO_3 [12–15]. The DFT+U+NEB study by Shin *et al.* showed that, for Li^+ migrating in the presence of a single Li vacancy, the calculated barriers are 0.5–0.8 eV for intralayer hops and 0.64–0.65 eV for interlayer hops [12]. They further found that if Li^+ migrates adjacent to a Li divacancy, the intralayer barrier drops to about 0.38 eV and the interlayer barrier to about 0.18 eV, while in the presence of a Li trivacancy the intralayer barrier can fall to ∼ 0.05 eV and the interlayer hop becomes effectively barrierless [12]. When compared with the microscopic (0.156 eV) and macroscopic (0.46 eV) experimental activation energies discussed above [9, 10], the barriers for Li+ migration in the presence of a single vacancy warrant further examination. Moreover, Li divacancies and trivacancies are unlikely to be abundant in the low-delithiation limit of nearly stoichiometric powder samples, such as those employed in the μ^+SR and ac-impedance measurements of Sugiyama *et al.* and Nakamura *et al.* [9, 10].

A second limitation of much of the existing first-principles literature on Li_2MnO_3 is its treatment of magnetism. In previous DFT+U studies, calculations have been performed within spin-polarized DFT+U assuming ferromagnetic order [14, 16, 17], in magnetically ordered states with the underlying spin configuration left unspecified [12, 15], or in a fully nonmagnetic (spin-unpolarized) state [6, 18]. However, Li_2MnO_3 has a relatively low Néel temperature, $T_N \approx 36$ K [19, 20], and is paramagnetic under the conditions relevant for Li-ion diffusion experiments and battery operation. Nonmagnetic calculations suppress local Mn moments entirely, whereas a true paramagnet exhibits zero net magnetization only

as a result of thermal fluctuations of finite local moments. A finite-temperature framework that preserves local-moment physics- such as DFT combined with dynamical mean-field theory (DFT+DMFT) [21–24] - is therefore required to describe diffusion barriers in the experimentally relevant paramagnetic phase.

Owing to the low crystallographic symmetry of Li_2MnO_3 (space group $C2/m$, No. 12), standard Wannier projections in the DFT+DMFT framework often produce effective Hamiltonians with substantial off-diagonal matrix elements, which can hinder DMFT from correctly reproducing the insulating gap of Li_2MnO_3. In our recent DFT+DMFT study of Li_2MnO_3 [21], we identified an efficient strategy to accurately capture its electronic structure by diagonalizing the Mn-d block. This approach demonstrates the viability of a low-energy, d-only model for Li_2MnO_3, in which the resulting Wannier basis implicitly encodes Mn-d–O-p hybridization.

In this work, we address these issues by combining DFT+U, DMFT with a quantum Monte Carlo impurity solver, and NEB calculations for a single Li vacancy in paramagnetic Li_2MnO_3 at room temperature. We first construct migration pathways using DFT+U NEB for six representative intra- and interlayer hops, and then evaluate DMFT total energies along these geometries, allowing the correlated electronic configuration to relax at each image. Dynamical electronic correlations substantially reduce the activation energies for the lowest-barrier paths, yielding $E_a = 0.18$ eV for the lowest-E_a intralayer hop and $E_a = 0.50$ eV for the next-lowest intralayer path, while the barriers for the remaining paths within DMFT remain close to their DFT+U values. These two lowest barriers quantitatively reproduce the short-range activation energy from μ^+SR and the long-range activation energy from ac-impedance measurements, establishing a unified microscopic picture without invoking clustered vacancy configurations or strong extrinsic disorder.

II. COMPUTATIONAL METHODS

A. DFT+DMFT

We employ the non-charge-self-consistent DFT+DMFT method [25, 26] for DFT-relaxed structures. For the underlying DFT calculations, we use the projector augmented wave (PAW) method [27] and the revised generalized gradient approximation (GGA) functional proposed by Perdew *et al.* (PBEsol) [28], as implemented in VASP [29]. A spin-independent version of the exchange-correlation functional is employed. A plane-wave basis with a kinetic-energy cutoff of 500 eV is used. We used 48-atom supercells (i.e., $1 \times 2 \times 2$ unit cells), which contain 8 Mn atoms, together with Γ-centered **k**-point meshes of size $10 \times 5 \times 5$. Atomic positions were relaxed until the residual forces were less than 0.01 eV/Å, and the residual stress was reduced below 0.02 kB.

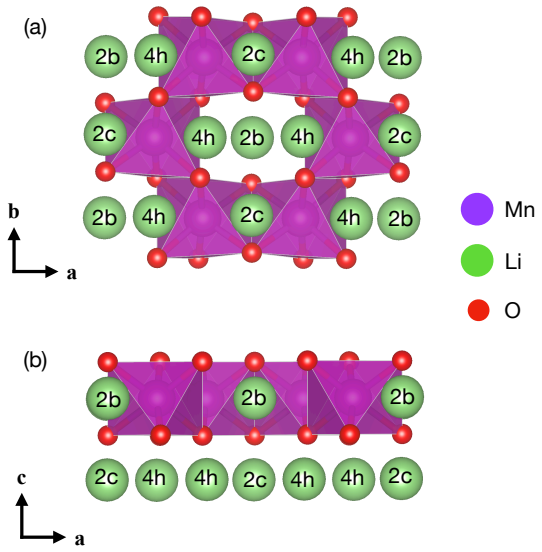

FIG. 1. Atomic structure of Li_2MnO_3 with positions of Li ions.

We solve the many-body problem in the Mn 3d-only manifold. The DFT+DMFT calculation proceeds as follows. First, we solve the non-spin-polarized Kohn–Sham equations within DFT using VASP. Second, we construct a localized-basis Hamiltonian for the Mn 3d bands by generating maximally localized Wannier functions (MLWFs)[30] from the nonmagnetic DFT band structure. For the d-only basis, the energy window is chosen from $E_F - 2.0$ eV to $E_F + 4.0$ eV. For the main DFT+DMFT calculations, we use $U = 2.5$ eV and $J = 0.9$ eV for the Mn-d correlated subspace. This choice is consistent with our previous d-only study, which showed that $U = 2.0$–2.5 eV reproduces the experimental band gap E_g.[21] Finally, we solve the DMFT self-consistent equations for the correlated subspace of Mn 3d Wannier orbitals using the continuous-time quantum Monte Carlo (CTQMC) impurity solver.[31, 32]

In the present non-charge-self-consistent DFT+DMFT implementation, total energies are available but ionic forces are not. Therefore, the migration pathways and saddle-point geometries used in this work were optimized at the DFT+U level. The DFT+DMFT total energies were then evaluated on the corresponding fixed NEB geometries for the initial, saddle-point, and final images, after convergence of the correlated electronic state for each configuration. Accordingly, the present workflow is designed to assess how finite-temperature dynamical correlations renormalize the energetics along a common ionic pathway, rather than to perform a fully DFT+DMFT-relaxed NEB optimization.

For the initial, saddle-point, and final images, we tested several different initial conditions for the DFT+DMFT calculation, differing in the choice of Mn-centered correlated subspace used to construct the ini-

tial guess, because the d-only DFT+DMFT setup can converge to multiple low-energy solutions for the same ionic geometry. We retained the lowest-energy converged solution for the subsequent analysis. In practice, the numerical convergence of the CTQMC-based DFT+DMFT calculations was monitored from the stability of the impurity-energy contribution to the total energy over successive DMFT iterations. Once its residual oscillation was within approximately 10 meV, the solution was regarded as converged, and the final total energy was obtained by averaging over the last 10 DMFT iterations. The impurity occupancy N_d was typically even more stable, varying only at the level of $\sim 10^{-3}$.

The rotationally invariant Coulomb interaction in the form of the Slater-Kanamori interaction Hamiltonian [33–35] is

$$\begin{aligned}\hat{H}_{\mathrm{SK}} = U\sum_{\alpha}\hat{n}_{\alpha\uparrow}\hat{n}_{\alpha\downarrow} + \frac{1}{2}\sum_{\alpha\neq\beta}\sum_{\sigma\sigma'}\left(U' - J\delta_{\sigma\sigma'}\right)\hat{n}_{\alpha\sigma}\hat{n}_{\beta\sigma'} \\ - \sum_{\alpha\neq\beta}\left(Jc^{\dagger}_{\alpha\uparrow}c_{\alpha\downarrow}c^{\dagger}_{\beta\downarrow}c_{\beta\uparrow} + J'c^{\dagger}_{\beta\uparrow}c^{\dagger}_{\beta\downarrow}c_{\alpha\uparrow}c_{\alpha\downarrow}\right).\end{aligned} \tag{1}$$

Here, c_σ and $c^{\dagger}_{\sigma}$ denote the fermion annihilation and creation operators, where σ is the spin. U denotes an intra-orbital density-density interaction parameter, U' is an inter-orbital density-density interaction parameter, J is a spin-flip interaction parameter, and J' is a pair-hopping interaction parameter. $U' = U - 2J$ and $J' = J$ are due to rotational invariance.

Within DFT+DMFT framework [26], the self-energy convergence is achieved when $\Sigma^{\mathrm{loc}}(i\omega) = \Sigma^{\mathrm{imp}}(i\omega)$, where $\Sigma^{\mathrm{loc}}(i\omega)$ and $\Sigma^{\mathrm{imp}}(i\omega)$ are local and lattice self-energies, respectively, and $i\omega$ is imaginary frequency. Σ is approximated as a local quantity in the correlated subspace. DFT+DMFT total energy is given by

$$\begin{aligned}E^{\mathrm{TOT}} =& E^{\mathrm{DFT}}(\rho) + \sum_{m,\mathbf{k}}\epsilon_m(\mathbf{k})\cdot\left[n_{mm}(\mathbf{k}) - f_m(\mathbf{k})\right] \\ &+ E^{\mathrm{POT}} - E^{\mathrm{DC}},\end{aligned} \tag{2}$$

where E^{DFT} is the total energy from non spin-polarized DFT, and $\epsilon_m(\mathbf{k})$ are the DFT eigenvalues. $n_{mm}(\mathbf{k})$ and $f_m(\mathbf{k})$ are the diagonal DMFT occupancy matrix element and Fermi function, respectively, for mth KS band and momentum $\mathbf{k}$. The potential energy E^{POT} is calculated by using Migdal-Galiski formula [36]:

$$E^{\mathrm{POT}} = \frac{1}{2}\sum_{\omega}\left[\Sigma^{\mathrm{loc}}(i\omega)\cdot G^{\mathrm{loc}}(i\omega)\right]. \tag{3}$$

Here, the local Green's function is simplified by $G^{\mathrm{loc}}(i\omega) = \sum_{\mathbf{k}} G^{\mathrm{loc}}(\mathbf{k}, i\omega)$.

To obtain the spectral function, the maximum entropy method is used for the analytic continuation. Spectral function $A(\omega)$ is given by

$$A(\omega) = -\frac{1}{\pi}\mathrm{Im}\Big[\sum_{\mathbf{k}} G^{\mathrm{loc}}(\mathbf{k},\omega)\Big]. \tag{4}$$

Large off-diagonal terms in the Hamiltonian can lead to significant errors within the DMFT method, as continuous time quantum Monte Carlo (CTQMC) only treats the diagonal terms to circumvent the sign problem. The non-parallel alignment of the cartesian axes of the Wannier orbitals and the directions of the Mn-O bonds arises from the C_{2h} point group symmetry of the MnO6 octahedron [Fig. 1]. In cases where the point group symmetry of the transition metal (TM) octahedron is non-cubic, such as trigonal or monoclinic, there is a substantial mixing of the d basis (d_{xy}, d_{xz}, d_{yz}, d_{z^2}, $d_{x^2-y^2}$), as these bases are defined within the cubic crystal field framework. Consequently, the off-diagonal terms of the Wannier Hamiltonian with the cubic d orbital basis become significant, leading to errors within the DMFT calculations. To resolve this issue, we diagonalize Mn d blocks of the Hamiltonian by applying a unitary rotation matrix, which is successful to reproduce the experimental energy gap [21].

Within DMFT, number of d electrons in Mn (N_d), is computed from the local Green function $G^{\mathrm{loc}}(\mathbf{k}, \mathbf{k}', i\omega)$:

$$N_d = \sum_{a,\omega}\sum_{\mathbf{k},\mathbf{k}'}\mathrm{Im}\big\{[\phi^a_d(\mathbf{k})]^* G^{\mathrm{loc}}(\mathbf{k},\mathbf{k}',i\omega)\phi^a_d(\mathbf{k}')\big\}, \tag{5}$$

where $\phi^a_d(\mathbf{k})$ is the normalized d-orbital wavefunction, which is transformed from the wavefunction in the real space $\phi^a_d(\mathbf{r})$ with the center of coordinates $\mathbf{r}$ on a transition metal ion.

B. DFT+U and atomic structures

The GGA+U scheme within the rotationally invariant formalism together with the fully localized limit double-counting formula [37] is used to study the effect of electron interactions. We used U=4 and J= 0 unless specified. Projected density of states (PDOS) are obtained by the spherical harmonic projections inside spheres around each atom. Wigner-Seitz radii of 1.323 Å were used for the projection of Mn atoms, respectively, as implemented in the VASP-PAW pseudopotential.

Both spin-unpolarized and spin-polarized versions of the exchange–correlation functional were employed in the DFT+U calculations. For each magnetic configuration, the structure was fully relaxed, including both internal atomic coordinates and lattice stresses. We used a 1×1×2 supercell to compare the relative energies of different magnetic phases within DFT+U, and a 1×2×2 supercell to compute Li migration paths in both the DFT+U and DMFT calculations.

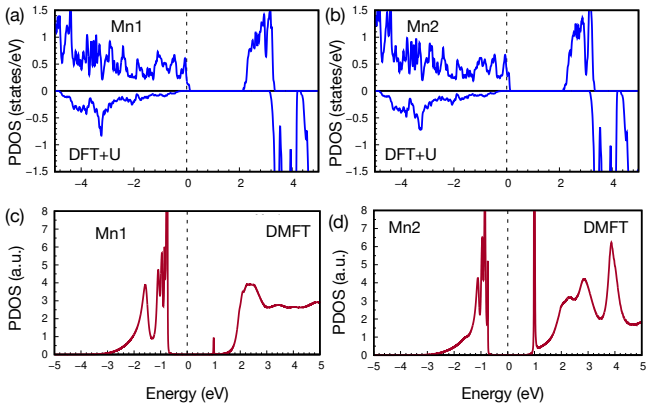

FIG. 2. Electronic structure of Li_2MnO_3 with a single Li vacancy from DFT+U and DMFT. (a,b) DFT+U projected density of states (PDOS) onto Mn1 and Mn2 d states. (c,d) DMFT PDOS projected onto the Mn-d–like correlated subspace on Mn1 and Mn2. Mn1 and Mn2 denote inequivalent Mn sites. We caution that in the downfolded DMFT setup the correlated orbitals are Mn-d–like Wannier functions that implicitly include Mn–O hybridization; therefore changes in the projected Mn-d occupancy reflect the effective low-energy description and should not be interpreted as a direct oxidation-state assignment in the full p–d manifold.

III. RESULTS AND DISCUSSION

A. Electronic structure of Li_2MnO_3 with single Li vacancy

First, we study the electronic properties of Li_2MnO_3 with a single Li vacancy using DFT+U. There are three distinct Li sites, 2b, 4h, and 2c, as shown in Fig. 1. Using a $1 \times 1 \times 2$ supercell containing four Mn atoms, we compare the total energies of four collinear magnetic configurations: ferromagnetic (FM), A-type antiferromagnetic (A-AF), C-type antiferromagnetic (C-AF), and G-type antiferromagnetic (G-AF), for different Li-vacancy positions, where A-, C-, and G-type denote antiferromagnetic alignment along one, two, and three crystallographic directions defined by the conventional a, b, and c lattice vectors. For each Li-vacancy configuration, the FM phase is more stable than the AF phases by 14–182 meV (see Table I in Appendix). Thus, in the Li-diffusion calculations employing a larger $1 \times 2 \times 2$ supercell, we adopt the FM configuration.

Figure 2 shows the projected density of states (PDOS) onto Mn d states in Li_2MnO_3 with a single Li vacancy. Removing one Li atom reduces the electron count by one (creating a single hole). We examine two inequivalent Mn sites: Mn1, adjacent to the vacancy (Mn1–Li_{vac} = 2.89 Å), and Mn2, farther away (Mn2–Li_{vac} = 3.90 Å). Within DFT+U, the Mn-projected spectra at Mn1 and Mn2 are nearly indistinguishable [Fig. 2(a,b)]: no sharp in-gap state forms, and the weight near the valence-band maximum (VBM) remains broadly distributed. Consistently, the integrated Mn-d occupations vary only weakly, N_d(Mn1) = 4.88 and N_d(Mn2) = 4.89, indicating that the vacancy does not produce a strongly site-selective change within the Mn-d manifold at this level of theory. In line with prior DFT+U and hybrid-functional studies [6, 16, 38], the vacancy-induced change at the VBM is primarily associated with O 2p states (ligand-hole character), rather than the formation of a well-defined Mn^{5+} oxidation state.

In contrast, the d-only DMFT results [Fig. 2(c,d)] show a strongly site-dependent redistribution of spectral weight within the Mn-d–like correlated subspace. Relative to Mn1, Mn2 exhibits a pronounced depletion of occupied Mn-d weight together with an increase of unoccupied weight near E_F, while the Mn1-projected spectrum remains comparatively unchanged. The corresponding Mn-d–like occupations are N_d(Mn1) = 3.00 and N_d(Mn2) = 2.01 (nominal values within the reduced correlated subspace), i.e., the dominant reduction of the Mn-d–like occupation occurs on Mn2. We emphasize that in this downfolded description the O degrees of freedom are not treated explicitly; their influence is incorporated through renormalized crystal fields and hoppings of the Mn-d–like Wannier basis. Therefore, the apparent Mn-centered site dependence should be interpreted as a property of the effective low-energy representation, not as direct evidence for a literal integer-valence Mn oxidation-state change in the full p–d electronic structure. A definitive real-space assignment of oxygen- versus manganese-centered hole character would require a fully charge-self-consistent p–d correlated subspace, which is considerably more computationally demanding and is left for future work. This difference between DFT+U and DMFT in the correlated-subspace charge rearrangement in the presence of the vacancy also suggests that the two methods can yield different Li-ion migration barriers. Since DMFT modifies the electronic response along the migration coordinate via dynamical correlations (as quantified below through the total-energy decomposition), the resulting migration barrier can differ from that obtained in static DFT+U.

B. Li-ion migration barriers: DFT+U versus DMFT

Next, we analyze Li^+ migration in Li_2MnO_3 using DFT+U and DFT+DMFT. We consider six symmetry-inequivalent pathways defined in Fig. 3: four *intralayer* hops, (i) $4h-T_{4g}^{Li}-4h$, (ii) $4h-T_{2b}^{Li}-4h$, (iii) $4h-T_{4g}^{Li}-2c$, (iv) $4h-T_{2b}^{Li}-2c$, and two *interlayer* hops, (v) $2b-T_{2b}^{Li}-2c$, and (vi) $2b-T_{2b}^{Li}-4h$. These paths are similar to those considered in a previous DFT+U study.[12]

The corresponding activation energies E_a are summarized in Fig. 5 (blue: DFT+U; red: DFT+DMFT). We first obtain the migration pathways and saddle-point geometries using NEB within spin-polarized DFT+U, and

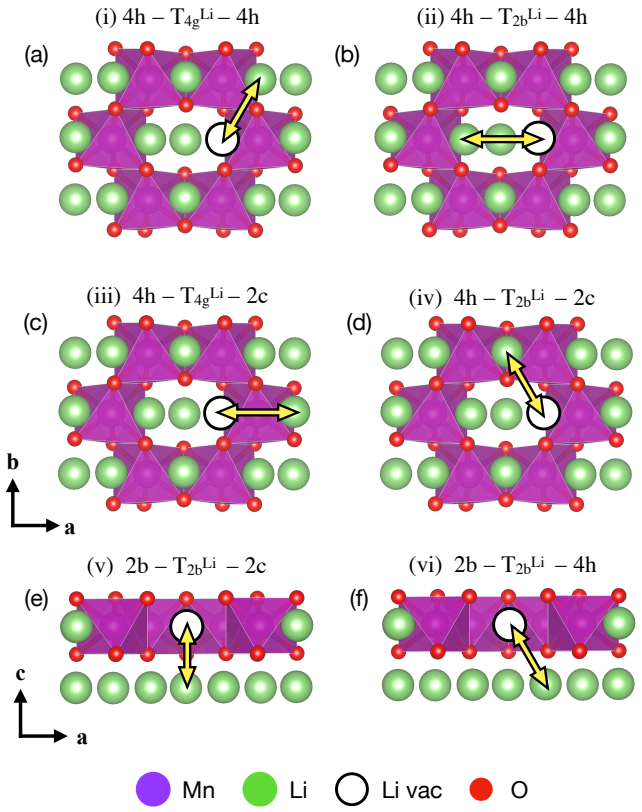

FIG. 3. Diffusion path of single Li vacancy in Li_2MnO_3. (a)-(d) intra layer diffusion. (e)-(f) inter layer diffusion.

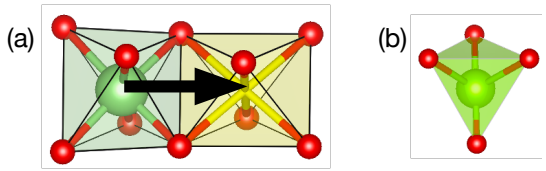

FIG. 4. (a) Diffusion path (*ii*) of single Li vacancy in Li_2MnO_3, and (b) LiO_4 tetrahedral structure at the saddle point.

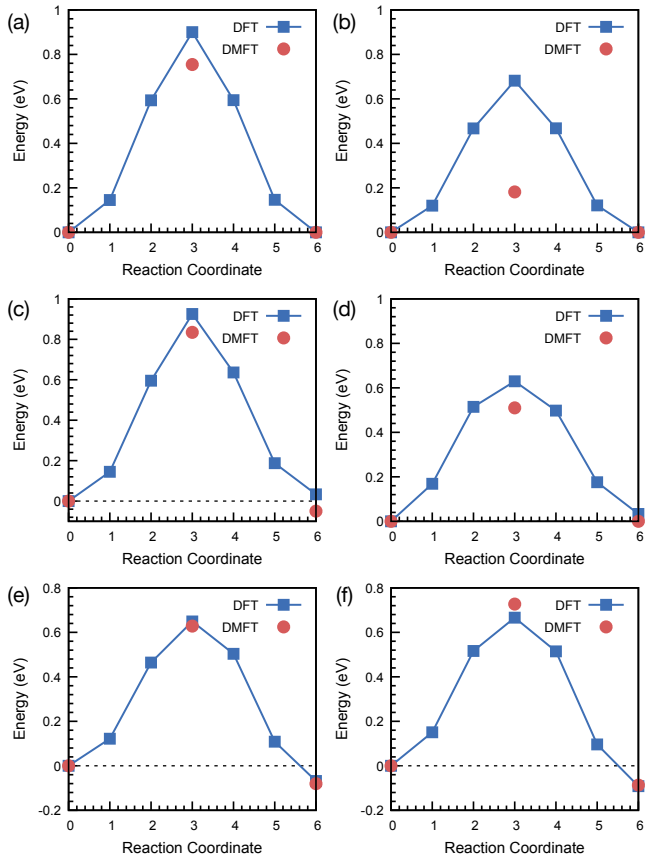

FIG. 5. (a)–(f) Migration barriers for a single Li vacancy in Li_2MnO_3 along pathways (i)–(vi), respectively.

then evaluate the DFT+DMFT total energies of the initial, final, and saddle-point configurations on these fixed geometries. Because the present DFT+DMFT implementation does not provide ionic forces, the present comparison does not constitute a fully DFT+DMFT-relaxed NEB calculation. Instead, it isolates how finite-temperature dynamical correlations modify the relative energetics along a common migration pathway. For each NEB image, we also tested multiple initial guesses and retained the lowest-energy converged DFT+DMFT solution in the subsequent analysis.

Within DFT+U, the migration barriers for intralayer diffusion are E_a = 0.63–0.93 eV. In all cases, Li^+ migrates via the tetrahedral interstitial site (T), forming a LiO_4 tetrahedron at the saddle point, as shown in Fig. 4, consistent with previous work [12]. The barriers along paths (i) and (iii) are relatively large, E_a = 0.90 and 0.93 eV, respectively, in reasonable agreement with the earlier DFT+U values of 0.78 and 0.80 eV [12]; the remaining differences are likely due to details of the computational setup (e.g., supercell size and choice of parameters). In contrast, the barriers along paths (ii) and (iv) are lower, E_a = 0.68 and 0.63 eV, indicating that path (iv) provides the lowest intralayer migration barrier. The earlier DFT+U study also found E_a = 0.60 and 0.56 eV for paths (ii) and (iv), respectively, likewise identifying path (iv) as the lowest-barrier pathway. For interlayer diffusion within DFT+U, the barriers are E_a = 0.65 and 0.67 eV for paths (v) and (vi), respectively, which are slightly larger than the lowest intralayer diffusion barrier.

Next, we evaluate E_a within DFT+DMFT at 300 K in the paramagnetic phase. As in DFT+U, the lowest-E_a diffusion paths are (ii) $4h-T_{2b}^{Li}-4h$ and (iv) $4h-T_{2b}^{Li}-2c$, but DFT+DMFT notably reduces the corresponding barriers, as shown in Fig. 5. The DFT+DMFT activation energies for paths (ii) and (iv) are 0.18 and 0.50 eV, respectively, while for the remaining paths the DFT+U and DFT+DMFT barriers differ by only 0.02–0.15 eV.

We note that, in the present DFT+DMFT setup, the correlated subspace is defined by Mn-d-like Wannier functions that implicitly include Mn–O hybridization; consequently, the vacancy-induced charge rearrangement is described within this effective low-energy manifold.

As a limited check of the interaction-parameter dependence, we also performed additional DFT+DMFT calculations for a smaller $1 \times 1 \times 2$ supercell by varying the Mn-d interaction strength from $U = 2.0$ to $U = 2.5$ eV at fixed $J = 0.9$ eV. We focus on this range because, in our previous d-only study, $U = 2.0$–2.5 eV reproduced the experimental band gap reasonably well.[21] For representative migration pathways in the smaller supercell, the resulting activation energies change only modestly over this range of U, typically by at most a few hundredths of an eV. Thus, within this physically motivated parameter range, increasing U leads only to a modest quantitative change in E_{a}. A full interaction-parameter scan for the larger supercell used in the main text was not attempted because of the computational cost.

The lowest barrier of 0.18 eV corresponds to a short-range Li jump between neighboring sites within the Li_2MnO_3 region. This value is close to the experimental activation energy $E_a = 0.156$ eV obtained from μ^+SR measurements, which probe local Li self-diffusion in nearly stoichiometric Li_2MnO_3 powders [10]. Our DFT+DMFT results therefore suggest that the experimentally observed short-range activation scale can be rationalized by single-vacancy migration along the lowest-barrier pathway in the paramagnetic phase, without invoking Li divacancies or trivacancies.

From ac-impedance measurements on Li_2MnO_3 powder samples, which probe long-range Li-ion transport, Nakamura *et al.* reported an activation energy of $E_a = 0.46$ eV at 900 °C [9]. In our DFT+DMFT barrier landscape, the 0.18 eV hop alone does not form a percolating pathway for net Li transport out of the Li_2MnO_3 region [Fig. 5(b)], so long-range migration requires additional hops. Among these, the intralayer path (iv) has the lowest barrier, $E_a = 0.50$ eV, whereas the other relevant paths are higher. Thus, an energetically favorable long-range route consists of many low-barrier 0.18 eV hops combined with occasional 0.50 eV hops, for example $4h - T_{2b}^{\mathrm{Li}} - 4h - T_{2b}^{\mathrm{Li}} - 2c$, and the overall rate is controlled by the larger barrier, $E_a \approx 0.50$ eV. Despite the different experimental temperature, this controlling barrier is of the same order as the activation energy extracted from ac-impedance measurements, indicating a comparable bottleneck scale for long-range transport.

To clarify the origin of the reduced E_a within DFT+DMFT, we analyze the change in the total energy E^{TOT} [Eq. (2)] between the initial and saddle-point configurations for the lowest-barrier path, path (ii). For the underlying DFT contribution E^{DFT}, the saddle point lies 0.678 eV above the initial state. By contrast, the DFT+DMFT eigenvalue-correction term, $\sum_{m,\mathbf{k}} \epsilon_m(\mathbf{k})\,[n_{mm}(\mathbf{k}) - f_m(\mathbf{k})]$, substantially stabilizes the saddle point: this term is lower at the saddle point than at the initial configuration by 0.506 eV, thereby providing the dominant reduction of the net migration barrier. The remaining terms in Eq. (2) are comparatively small: E^{POT} is higher at the saddle point by only 0.070 eV, and E^{DC} changes by merely -0.45 meV. Thus, for path (ii), the barrier lowering within DFT+DMFT is dominated by the eigenvalue-correction term rather than by changes in the interaction or double-counting energies.

A useful contrast is provided by path (iii), for which the underlying DFT contribution to the barrier is similarly large, 0.790 eV, but the DFT+DMFT corrections remain very small. In this case, the eigenvalue-correction term changes by only +0.028 eV between the initial and saddle-point configurations, while E^{POT} and E^{DC} vary by just 0.006 and 0.004 eV, respectively. The comparison between paths (ii) and (iii) therefore shows that the pronounced suppression of E_a is strongly path dependent. In particular, path (ii) exhibits a large negative eigenvalue correction, whereas path (iii) does not, despite their similarly large underlying DFT barriers.

This difference correlates with the local registry of the migrating Li at the saddle point relative to the surrounding MnO_6 network. For path (ii), the migrating Li passes through a relatively open region of the Li sublattice, near a Li-centered hexagonal arrangement, so that there is no Mn ion located directly above or below the saddle-point Li. Consistent with this geometry, the nearest Li–Mn distance is relatively long, 3.254 Å. By contrast, for path (iii) the saddle-point Li lies much more directly beneath nearby MnO_6 octahedra, with two short Li–Mn distances of 2.514 and 2.596 Å. Path (iv) appears intermediate between these limits: its saddle-point Li also passes near a Li-centered hexagonal region, but with a less open local environment than in path (ii), and its shortest Li–Mn distance is correspondingly intermediate at 3.030 Å. Thus, the local registry of the saddle-point Li relative to the MnO_6 network correlates with the magnitude of the DFT+DMFT barrier renormalization, suggesting that the more open local environment of path (ii) is more effectively stabilized within the correlated electronic description than the corresponding saddle points of paths (iii) and (iv).

IV. CONCLUSION

In this work, we investigated Li-ion migration in Li_2MnO_3 by combining DFT+U, DFT+DMFT (with a continuous-time quantum Monte Carlo solver), and nudged-elastic-band (NEB) calculations for a single Li vacancy in the paramagnetic phase. By evaluating DMFT total energies on the fixed DFT+U NEB geometries for six representative intra- and interlayer paths—and optimizing the correlated electronic state at each NEB image—we find that dynamical correlations reduce the activation energies for the lowest-barrier paths to $E_a = 0.18$ eV for path (ii) and $E_a = 0.50$ eV for path (iv), while leaving the other paths largely unchanged relative

to DFT+U. The lowest barrier, $E_a = 0.18$ eV, is close to the microscopic activation energy for short-range Li self-diffusion extracted from μ^+SR measurements on nearly stoichiometric Li_2MnO_3 powders, suggesting that the local activation scale can be rationalized by single-vacancy migration along path (ii) in a paramagnetic host, without invoking Li divacancies or trivacancies.

Long-range transport, on the other hand, necessarily involves sequences of hops that combine low-barrier (0.18 eV) and higher-barrier (0.50 eV) steps; within such a network, the effective activation energy is controlled by the larger barrier, $E_a \approx 0.50$ eV. Despite the different experimental temperature, this controlling scale is of the same order as the macroscopic activation energies obtained from ac-impedance measurements on ceramic powders. Our results also indicate that interpretations based solely on interlayer diffusion are too restrictive, and that a mixture of intralayer processes is required to reconcile local and macroscopic probes.

These findings highlight the importance of beyond-DFT treatments for ionic diffusion in correlated oxides, and motivate future extensions to higher vacancy concentrations and mixed-cation Li-rich layered cathodes. In particular, extending the present framework to regimes where oxygen redox becomes active will be essential for assessing how lattice defects, charge redistribution, and dynamical correlations jointly influence transport and stability.

V. ACKNOWLEDGMENT

We acknowledge financial support from the U.S. Department of Energy, Office of Science, Office of Basic Energy Sciences, Materials Science and Engineering Division. We gratefully acknowledge the computing resources provided on Improv, a high-performance computing cluster operated by the Laboratory Computing Resource Center at the Argonne National Laboratory.

[1] J. B. Goodenough and Y. Kim, Chemistry of Materials **22**, 587 (2010).
[2] J. B. Goodenough and K.-S. Park, Journal of the American Chemical Society **135**, 1167 (2013), pMID: 23294028, https://doi.org/10.1021/ja3091438.
[3] A. Manthiram, ACS Central Science **3**, 1063 (2017).
[4] A. Manthiram, Nature Communications **11**, 1550 (2020).
[5] N. Yabuuchi, K. Yoshii, S.-T. Myung, I. Nakai, and S. Komaba, Journal of the American Chemical Society **133**, 4404 (2011), pMID: 21375288, https://doi.org/10.1021/ja108588y.
[6] D.-H. Seo, J. Lee, A. Urban, R. Malik, S. Kang, and G. Ceder, Nature Chemistry **8**, 692 (2016).
[7] D. Ye and L. Wang, Materials Technology: Advanced Performance Materials **29**, A59 (2014).
[8] G. Liu and S. Zhang, International Journal of Electrochemical Science **11**, 5545 (2016).
[9] K. Nakamura, H. Hirano, Y. Michihiro, and T. Moriga, Solid State Ionics **181**, 1359 (2010).
[10] J. Sugiyama, K. Mukai, H. Nozaki, M. Harada, M. Månsson, K. Kamazawa, D. Andreica, A. Amato, and A. D. Hillier, Phys. Rev. B **87**, 024409 (2013).
[11] H. Yu, Y. Wang, D. Asakura, E. Hosono, T. Zhang, and H. Zhou, RSC Advances **2**, 8797 (2012).
[12] Y. Shin, H. Ding, and K. A. Persson, Chem. Mater. **28**, 2081 (2016).
[13] F. Kong, R. C. Longo, M.-S. Park, J. Yoon, D.-H. Yeon, J.-H. Park, W.-H. Wang, S. KC, S.-G. Doo, and K. Cho, **3**, 8489, publisher: The Royal Society of Chemistry.
[14] S. Wang, J. Liu, and Q. Sun, J. Mater. Chem. A **5**, 16936 (2017).
[15] T. Sarkar, K. R. Prakasha, M. D. Bharadwaj, and A. S. Prakash, Phys. Chem. Chem. Phys. **19**, 31724 (2017).
[16] R. Xiao, H. Li, and L. Chen, Chemistry of Materials **24**, 4242 (2012).
[17] H. Chen and M. S. Islam, Chemistry of Materials **28**, 6656 (2016).
[18] K. Hikima, K. Shimizu, H. Kiuchi, Y. Hinuma, K. Suzuki, M. Hirayama, E. Matsubara, and R. Kanno, Journal of the American Chemical Society **144**, 236 (2022), pMID: 34957828, https://doi.org/10.1021/jacs.1c09087.
[19] P. Strobel and B. Lambert-Andron, Journal of Solid State Chemistry **75**, 90 (1988).
[20] S. Lee, S. Choi, J. Kim, H. Sim, C. Won, S. Lee, S. A. Kim, N. Hur, and J.-G. Park, Journal of Physics: Condensed Matter **24**, 456004 (2012).
[21] A. T. Lee, H. Park, and A. T. Ngo, Phys. Rev. B **108**, 205146 (2023).
[22] J. Molenda, P. Wilk, and J. Marzec, Solid State Ionics **146**, 73 (2002).
[23] D. M. Korotin, D. Novoselov, and V. I. Anisimov, Phys. Rev. B **99**, 045106 (2019).
[24] E. B. Isaacs and C. A. Marianetti, Phys. Rev. B **102**, 045146 (2020).
[25] H. Park, R. Nanguneri, and A. T. Ngo, Phys. Rev. B **101**, 195125 (2020).
[26] V. Singh, U. Herath, B. Wah, X. Liao, A. H. Romero, and H. Park, Computer Physics Communications **261**, 107778 (2021).
[27] P. E. Blöchl, Phys. Rev. B **50**, 17953 (1994).
[28] J. P. Perdew, A. Ruzsinszky, G. I. Csonka, O. A. Vydrov, G. E. Scuseria, L. A. Constantin, X. Zhou, and K. Burke, Phys. Rev. Lett. **100**, 136406 (2008).
[29] G. Kresse and D. Joubert, Phys. Rev. B **59**, 1758 (1999).
[30] N. Marzari, A. A. Mostofi, J. R. Yates, I. Souza, and D. Vanderbilt, Rev. Mod. Phys. **84**, 1419 (2012).
[31] K. Haule, Phys. Rev. B **75**, 155113 (2007).
[32] E. Gull, A. J. Millis, A. I. Lichtenstein, A. N. Rubtsov, M. Troyer, and P. Werner, Rev. Mod. Phys. **83**, 349 (2011).
[33] J. C. Slater, Phys. Rev. **82**, 538 (1951).
[34] J. Kanamori, Prog. Theor. Phys. **30**, 275 (1963).
[35] A. Georges, L. d. Medici, and J. Mravlje, Annu. Rev. Condens. Matter Phys. **4**, 137 (2013).
[36] V. Galitskii and A. Migdal, me Teoret. Fiz **34**, 96 (1958).

[37] A. I. Liechtenstein, V. I. Anisimov, and J. Zaanen, Phys. Rev. B **52**, R5467 (1995).
[38] K. Hoang, Phys. Rev. Appl. **3**, 024013 (2015).

VI. APPENDIX A

TABLE I. Relative energies (in eV) of collinear magnetic configurations within DFT+U for different Li-vacancy positions in the $1\times1\times2$ supercell. Here E denotes the total energy of a given configuration, $\Delta E = E - E_{\rm min}$ is measured with respect to the global ground state (FM with a Li vacancy at the $2b$ site), and $\delta E = E - E_{\rm FM}$(Li-vac) is measured with respect to the FM state for the same Li-vacancy position.

Li-vac site	Magnetic order	ΔE (eV)	δE (eV)
$2b$	FM	0.000	0.000
	A-AF	0.014	0.014
	C-AF	0.140	0.140
	G-AF	0.145	0.145
$4h$	FM	0.065	0.000
	A-AF	0.079	0.065
	C-AF	0.179	0.165
	G-AF	0.196	0.182
$2c$	FM	0.043	0.000
	A-AF	0.086	0.043
	C-AF	0.218	0.175
	G-AF	0.216	0.173